ADVANCED MATERIALS
www.advmat.de

Quantification of Nano- and Mesoscale Phase Separation and Relation to Donor and Acceptor Quantum Efficiency, J_{sc}, and FF in Polymer:Fullerene Solar Cells

Wei Ma, John R. Tumbleston, Long Ye, Cheng Wang, Jianhui Hou, and Harald Ade**

Controlling the morphology of polymer/fullerene bulk heterojunction (BHJ) systems is one of the key strategies to obtain high power conversion efficiencies (PCE)[1–13] and has contributed significantly to the improvement of the PCE from 1% to ~9% in the last fifteen years.[14–19] Various parameters and methods employed have included the control of the donor:acceptor ratio,[20,21] the molecular weight,[22] the choice of the solvent,[5] thermal annealing,[23] solvent annealing,[24] and the use of solvent mixtures and additives.[25,26] The goal is to obtain a favorable morphology that provides a large interfacial area for exciton splitting and charge separation as well as pathways for charge transport to the electrodes and avoidance of bimolecular recombination by having high mobility and/or high purity.[2,18,27,28] Among these, using solvent mixtures and additives is often the most effective optimization strategy to get improved efficiency for a given material system.[5,25,29–31]

Expanding the canonical two-phase paradigm, complex three-phase, hierarchical morphologies including pure fullerene aggregates, pure polymer aggregates, and a mixed phase, which is thought to consist of dispersed fullerene in mostly amorphous polymer, have been observed or inferred in several cases.[5,8,32–35] This has caused a re-evaluation of the actual morphologies, initiated by the observation of miscibility of fullerene in many donor polymers.[8,23,36–38] Given the apparent universality of miscibility and thus the likely presence of a mixed phase, the presence of at least one, if not two pure phases was thought to be beneficial for good fill factor by reducing bimolecular recombination.[32,39,40] More recently, it has been argued that the pure phases have different energetic levels due to more extended conjugation/aggregation. The electron affinity of pure fullerene domains is likely to be higher than that of fullerene in mixed domains,[33] whereas pure polymers have longer conjugation lengths and lower ionization potentials than an amorphous polymer phase.[41,42] This generally favorable electronic landscape makes it more probable for electrons and holes to exit the mixed regions and move to purer fullerene and purer polymer domains, thus effectively confining the electrons in the purer donor and acceptor phase, respectively. Hence, a three-phase morphology of aggregated fullerene, pure polymer, and a mixed polymer:fullerene domain might be a more favorable morphology than initially thought, as long the pure fullerene and polymer phases are sufficiently connected (dispersed pure phases will trap holes or electrons).

Even within a three-phase morphology paradigm, due to the small exciton diffusion length of ca. 10 nm, small scale, nanophase separation has to be present for efficient exciton dissociation efficiency.[28,33,43,44] Hence, domain size is the most commonly investigated morphological factor in BHJ organic solar cells and its influence on device performance is widely considered critical.[5,13,23,45–48] Furthermore, it is assumed that high average purity will effectively reduce bimolecular recombination and consequently improve device performance.[23,49] For example, highly pure domains in poly[2,6-(4,8bis(2-(4,5-didecyl)thiophene)benzo[1,2-b:4,5-b′]dithiophene)-*alt*-3,7-(di(4-hexyl-2-thienyl))-naphtho[1,2-c:5,6-c]bis[1,2,5]thiadiazole)]-based PBDT-DTNT blends lead to reduced bimolecular recombination and thus improve the FF compared with less-pure domains in the 2,1,3-benzothiadiazole-based counterpart, PBDT-DTBT, blends film.[23] A similar observation is found in fluorine-substituted polymer based blends,[46,49] while Monte-Carlo simulations are also consistent with this argument.[44,50] On the other hand, if mixed domains larger than the exciton diffusion length are themselves too pure (i.e., have insufficient nanomorphology), insufficient percolation pathways can lead to reduced device performance as recently inferred by Bartelt et al.[34] and Ma and co-workers.[23,51] These studies reveal that average domain purity of the mixed phase may have a critical threshold value in some systems that yield maximized performance. However, a systematic understanding on this trade-off and its manipulation via solvent mixtures has not yet been achieved.

In order to start addressing these outstanding questions, we used six solvents mixtures based on chloroform (CF), dichlorobenzene (DCB) and 1,8-diiodooctane (DIO), yielding CF, DCB, DCB/CF, CF/DIO, DCB/DIO and DCB/CF/DIO to manipulate

Dr. W. Ma, Dr. J. R. Tumbleston, Prof. H. Ade
Department of Physics
North Carolina State University
Raleigh, NC 27695, USA
E-mail: harald_ade@ncsu.edu
L. Ye, Prof. J. Hou
State Key Laboratory of Polymer Physics and Chemistry
Beijing National Laboratory for Molecular Sciences
Institute of Chemistry
Chinese Academy of Sciences
Beijing 100190, China
E-mail: hjhzlz@iccas.ac.cn
L. Ye
University of Chinese Academy of Sciences
Beijing 100049, China
Dr. C. Wang
Advanced Light Source
Laurence Berkeley National Laboratory
Berkeley, California 94720, USA

DOI: 10.1002/adma.201400216

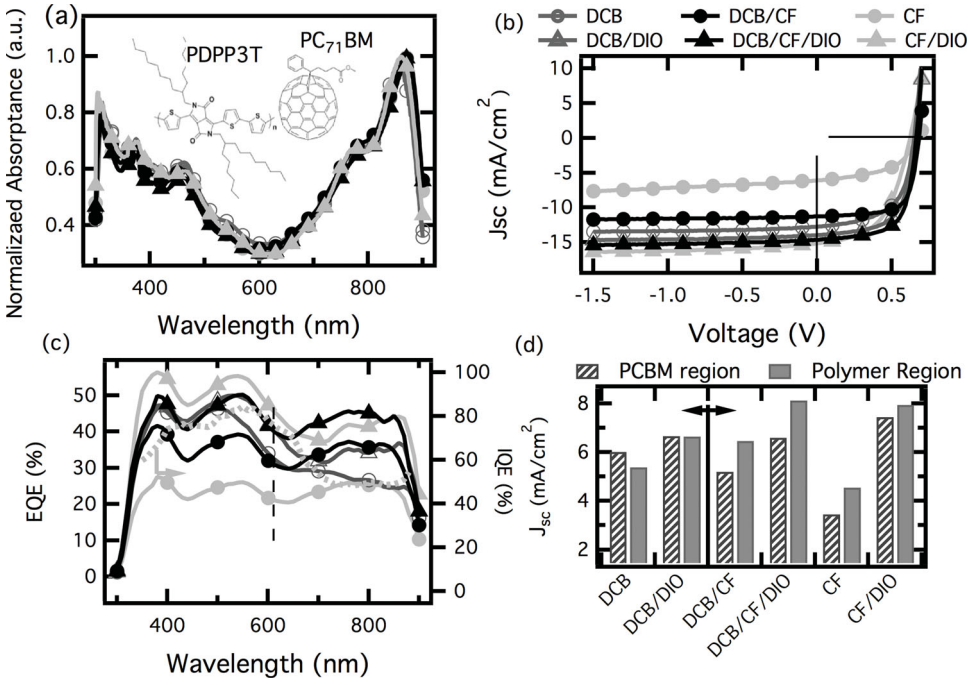

Figure 1. Characteristics for 120–140 nm thick PDPP3T:$PC_{71}BM$ devices processed from different solvents: DCB, DCB/DIO, DCB/CF, DCB/CF/DIO, CF and CF/DIO: a) UV–vis absorption spectra (chemical structure of PDPP3T and $PC_{71}BM$ inset), b) current–voltage characteristics under 1-sun illumination; c) external quantum efficiency (EQE) spectra of devices processed with different solvents, internal quantum efficiency (IQE) of blend films processed with CF/DIO are shown as dashed line. d) J_{sc} contribution from PCBM regions or PDPP3T regions. (On the left side of the solid line, no CF is used and $J_{sc:PCBM} > J_{sc:polymer}$, while on the right side of the solid line CF is used and $J_{sc:PCBM} < J_{sc:polymer}$).

the morphology of the promising low bandgap polymer poly[{2,5-bis(2-hexyldecyl)-2,3,5,6-tetrahydro-3,6-dioxopyrrolo[3,4-c]pyrrole-1,4-diyl}-*alt*-{[2,2′:5′,2″-terthiophene]-5,5″-diyl}] and [6,6]-phenyl C71 butyric acid methyl ester, PDPP3T:$PC_{71}BM$-based device. This complements a recent report on use of ternary solvents to optimize, for the time being, the same DPP based system.[25] However, rather than seeking to optimize performance, we use the systems to elucidate complex morphology–performance relations. The samples are freshly prepared to minimize the morphological changes prior to X-ray characterization, and showed similar performance to the prior study. With a novel multipeak-fitting analysis method, the length scale that characterizes polymer-rich and fullerene-rich domains (referred to as mesoscale) and the internal structure of polymer-rich phases (referred to as nanoscale) as well the average composition variations at these length scales are determined with resonant soft-X-ray scattering (R-SoXS).[5–7,25,52,53] The polymer aggregate structure as revealed by grazing-incidence wide-angle X-ray scattering (GIWAXS) corresponds to the R-SoXS revealed nanoscale. Anti-correlated composition variations are determined for the first time between the mesoscale phase separation and the nanoscale phase separation, as one would expect when $PC_{71}BM$ is moving from the nano- to the mesoscale. We find that the current density J_{sc} is strongly dependent on the nano-length-scale of the polymer-rich domains. The total photocurrent generated from $PC_{71}BM$ and polymer is considered separately and we find the nanophase plays an important role. Our studies support a morphology paradigm in actual devices in which a suitably mixed phase and percolation within a polymer-rich phase are critical in order to optimize performance within a given preparation protocol or materials system. Our work also suggests that solvent choice has selective impact on the polymer and fullerene quantum efficiency and that the PDPP3T: $PC_{71}BM$ system has not yet been optimized. Furthermore, we find that lack of high composition variations (i.e. purity) on either the mesoscale or nanoscale can negatively impact FF.

The UV–vis absorption spectra of PDPP3T:$PC_{71}BM$ (D/A ratio is 1:2) processed with the six solvent mixtures used are shown in **Figure 1**a. We note that the 120–140 nm thick films (details in **Table 1**) have a very broad response from 300 nm to 900 nm, where 300–620 nm is mainly covered by $PC_{71}BM$ absorption and 620–900 nm is highly absorbed in PDPP3T (except PDPP3T has a small absorption shoulder at 400 nm).[54] We note that there are no significant differences between any of the solvent mixtures, indicating that aggregation is very high for all devices, consistent with the work by Janssen et al. on lower molecular weight PDPP3T.[54] The polymer is thus strongly aggregated in blend films, likely resulting in pure polymer phases in blend films.

The device characteristics (*J*–*V*) are shown in Figure 1b and are summarized in Table 1 and are highly dependent on which solvent/additive mixture is used. For example, it is noted that J_{sc} can be significantly improved by adding the DIO additive in both pure host solvents and binary host solvents. The FF ranges from a poor 52.9% (CF/DIO) to an excellent 70.1% (DCB/CF) and has a complex dependence. The current density is relatively field-independent below 0 V. Overall, the highest PCE is presently obtained by the ternary solvent DCB/CF/DIO.

The external quantum efficiency (EQE) curves are shown in Figure 1c and, unlike the UV–vis spectra, are highly solvent

Adv. Mater. **2014**,
DOI: 10.1002/adma.201400216

Table 1. Performance and structure parameters for PDPP3T: $PC_{71}BM$ blend films processed with different solvents.

Solvent	d [nm]	V_{oc} [V]	J_{sc} [mA/cm^2]	FF [%]	PCE [%]	$J_{sc:PC71BM}$ [mA/cm^2]	$J_{sc:Poly}$ [mA/cm^2]	ξ_2 [nm]	$<\Delta c>_2$	ξ_3 [nm]	(100) coher. length	$<\Delta c>_3$	SIξ_3/TSI
DCB	140	0.65	12.4	58.9	4.74	4.74	6.02	109	0.57	26.2	22.1	0.24	0.16
DCB/DIO	120	0.66	14.0	62.4	5.75	5.75	6.66	140	0.58	36.9	34.7	1.00	0.46
DCB/CF	125	0.68	11.4	70.2	5.44	5.44	5.21	104	0.74	23.7	19.2	0.53	0.18
DCB/CF/DIO	125	0.66	15.0	66.0	6.51	6.51	6.60	109	0.87	27.3	26.6	0.41	0.15
CF	130	0.67	6.07	51.8	2.11	2.11	3.46	194	0.36	<10	10.1	NA	NA
CF/DIO	130	0.63	15.2	52.9	5.06	5.06	7.45	54	1	15.3	19.6	0.19	0.04

dependent. The internal quantum efficiency (IQE) is calculated for all blends (Figure S1). The example IQE (CF/DIO, highest J_{sc}) shown in Figure 1c, reveals that the IQE of the polymer is much lower than of the $PC_{71}BM$. Quantitative analysis of this effect has been performed by integrating the product of EQE and the solar spectrum in the range of 300–620 nm and 620–900 nm and referring to these quantities as $J_{sc:PCBM}$ and $J_{sc:polymer}$, respectively (Figure 1d and Table 1). Due to the absorption shoulder of the PDPP3T polymer at 400 nm, this separation is an estimate of the lower limit for the differences observed, a lower limit for the PDPP3T and an upper limit for the PCBM contribution, respectively. It is found that $J_{sc:PCBM}$ and $J_{sc:polymer}$ exhibit different solvent dependence. This indicates that the relative photocurrent contribution from PDPP3T or PCBM domains is strongly morphology dependent, which in turn is driven by the solvent mixture used. Mixtures that include CF have generally better EQE for the polymer but worse for the PCBM (shown right in Figure 1d), whereas mixtures with DIO have better EQE for both polymer and fullerene compared to w/o DIO.

The molecular order of the six PDPP3T:$PC_{71}BM$ blend thin films is characterized using grazing incidence wide-angle X-ray scattering (GIWAXS) (see Figure S2, Supporting Information). The in-plane (100) coherence length is revealed and tabulated in Table 1 with detailed analysis presented in the Supporting Information. Since GIWAXS probes only the molecular order between the same material, transmission R-SoXS is employed to probe in-plane composition variations over length scales spanning ca. 10–1000 nm.[5–7,25,52,53,55] A photon energy of 283 eV was selected to provide high polymer:fullerene contrast while reducing mass–thickness contrast[13] and avoiding high absorption above the absorption edges which can lead to beam damage[56] and fluorescence background. **Figure 2** shows the scattering profiles for the PDPP3T: $PC_{71}BM$ blends. Improved data and a novel analysis allow us to fit the scattering by a set of three log–normal distributions including a separate peak at high q (q_3) which modifies our prior analysis of this q-range (see Figure S4 in the Supporting Information for details).[25] It is noted that CF-cast sample data cannot be successfully fitted by three log–normal distributions in a manner consistent with the other five samples. We thus fit the high-q data with the scaling exponent function similar to our prior work.[25] The fitting for the DCB/DIO data is plotted in Figure 2a as an example and the fitted peaks are displayed on the bottom of Figure 2a. The very low q peak (q_1) has a nearly identical location as the scattering profile for 270 eV, an energy where the material:vacuum contrasts are dominant,[25] thus indicating that this peak corresponds to mass–thickness variations.

The separate peaks at medium and high q (q_2 and q_3) dominate the total scattering intensity (TSI) as can be readily observed in the linear-linear scattering plot shown in Figure 2b. The energy dependence of the scattering intensity (SI) of q_2 and q_3 follows the scattering contrast of PCBM-polymer (Figure 2c), demonstrating that these peaks measure the composition variations. q_2 reveals larger (i.e. mesoscale) separation and generally dominates the SI (see Table 1). Hence, it should correspond to polymer-rich and PCBM-rich phase separation. The scattering profiles represent the distribution function of spatial frequency, $s = q/2\pi$, of the samples. The median of the distribution s_{median} corresponds to the characteristic median length scale, ξ, of the corresponding distribution in real space with $\xi = 1/s_{median}$. From q_2, which corresponds to the peak with highest fractional SIξ_2, we obtain the polymer-rich and PCBM-rich phase separation length scale ξ_2. We find that blend films processed with DCB have a ξ_2 of ca. 109 nm. When 20% CF is added to DCB, ξ_2 slightly decreases to 104 nm. When 5% DIO is used, ξ_2 slightly increases compared to the pure DCB solvent sample. The effects of CF and DIO largely negate each other, and the mixture of CF and DIO in DCB (DCB/CF/DIO) does not alter ξ_2 compared to pure DCB. When CF is the majority solvent (i.e CF and CF/DIO), it induces the largest and the smallest length scale, respectively. Scanning transmission X-ray microscopy (STXM)[57] of the CF blend films reveals a length scale and low contrast that is consistent with the R-SoXS (see Figure S5, Supporting Information). STXM also reveals a low residual PCBM concentration of only 4.5% PCBM in a polymer matrix of aggressively thermally annealed blends for which the majority of the PCBM has segregated into huge agglomerates. This is one of the lowest residual values observed to date.[8,23,37,51,58] It indicates very low miscibility of the fullerene in the polymer, reflects the very large molecular weight (M_n = 780 kg/mol) and strong aggregation of the DPP used, and is one of the major driving forces for phase separation.

The high-q peaks from R-SoXS reveal a ξ_3 for DCB, DCB/DIO, DCB/CF, DCB/CF/DIO and CF/DIO of 26.2, 36.9, 23.7, 27.3 and 15.3 nm, respectively (Table 1). Although there appears to be a tiny shoulder in the CF data, no clearly quantifiable high-q peak is observed in the measured q range for CF, which could indicate ξ_3 is too small to be captured in this experiment or there is no well-defined second length scale of importance

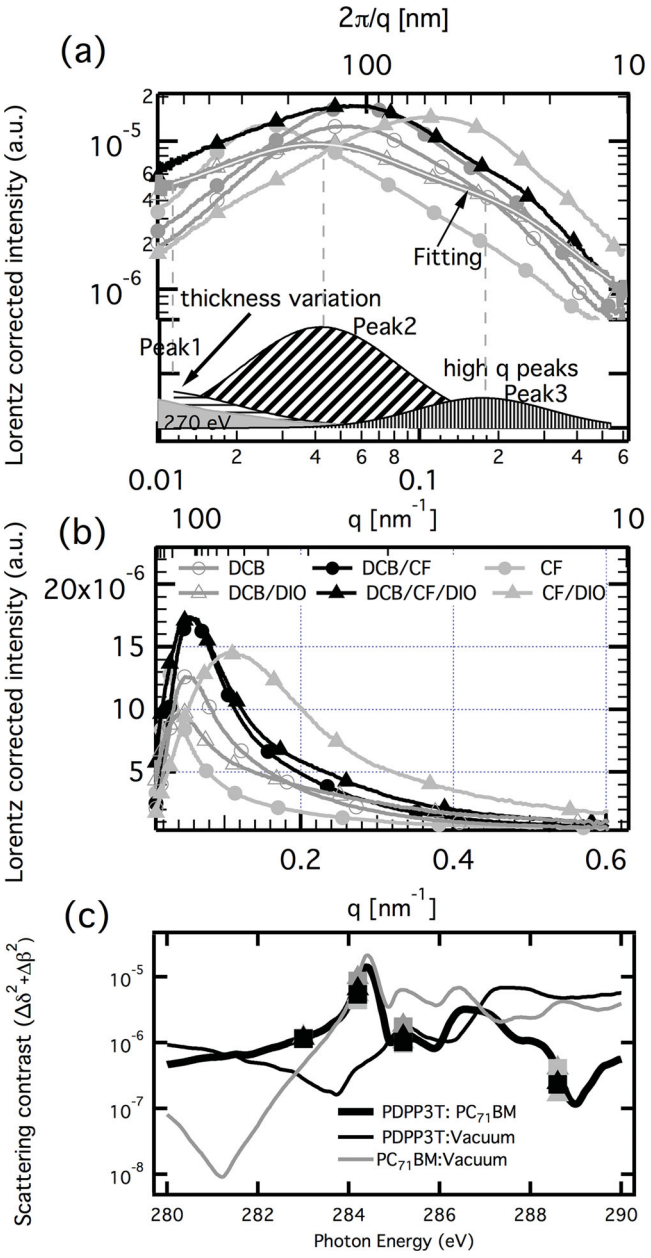

Figure 2. Lorentz corrected[59] R-SoXS scattering profiles (283 eV) of blend films processed from solvents as indicated. a) Log–log plot, with log–normal fits for the DCB/DIO samples on bottom. b) Lin–lin plot, the natural representation to visually judge the total scattering intensity (i.e., area under the curves), which is proportional to the average composition variations, $<\Delta c>$, over the lengthscale probed. c) The contrast function of PDPP3T:PCBM, PDPP3T:vacuum, and PCBM:vacuum along with the total scattering intensity TSI.

present in the CF blends. Importantly, the (100) in-plane coherent length revealed by GIWAXS is correlated to ξ_3 (see Table 1, and Figure S6a, Supporting Information). This constitutes the first time that a length-scale that measures only polymer related ordering (from WAXS) can be related to a length-scale arising from compositional variations (from R-SoXS). This provides additional details about OPV blend morphologies previously unobserved. The smallest coherence length by far is observed for CF blends, consistent with our inability to observe a high q R-SoXS peak.

The average composition variations of the samples at meso- and nano-length-scales are obtained by calculating the fractional R-SoXS SI of q_2 and q_3.[13,25] The average composition variations of the mesophase domains, $<\Delta c>_2$, for DCB, DCB/DIO, DCB/CF, DCB/CF/DIO, CF and CF/DIO scaled to the highest variations are 0.57, 0.58, 0.74, 0.87, 0.36 and 1, respectively (Table 1). The domains of CF thin films are very mixed, but when CF is mixed with other solvents, the domains can be effectively purified; for example, $<\Delta c>_2$ increases from 0.71 in DCB to 0.82 in DCB/CF. Purification also occurs when DIO is employed. Combining the purification effect of CF and DIO, the purest domains are achieved (for which $<\Delta c>_2$ is set to 1 as a reference). The average composition variations of the nanophase separation, $<\Delta c>_3$ are 0.24, 1, 0.53, 0.41 and 0.19 for DCB, DCB/DIO, DCB/CF, DCB/CF/DIO and CF/DIO, respectively, again scaled to the largest variations (results summarized in Table 1). With the exception of DCB, which is the least crystalline system along with CF, $<\Delta c>_2$ and $<\Delta c>_3$ are highly anticorrelated (see **Figure 3**b), representing a unique aspect of our measurements. This would be expected for similar overall morphologies, as the removal of PCBM from the nanophase to the PCBM-rich aggregated phase reduces the contrast from within the nanophase and increases the contrast between the PCBM-rich phase and the nanophase.

A self-consistent picture of most aspects of the morphology emerges (Figure 3a). The correlation of the (100) in-plane coherence length and ξ_3 (see Figure S6a, Supporting Information), the energy dependence and magnitude of SI and its subcomponent SI and the anti-correlation of $<\Delta c>_2$ and $<\Delta c>_3$ (see Figure 3b), reveal that the nanoscale separation is between pure polymer crystallites/aggregates and a mixed polymer:fullerene phase of low average PCBM concentration which together constitute the polymer-rich phase. Interestingly, the ratio of ξ_2/ξ_3 is close to 4 for all systems except for CF for which we cannot determine a meaningful nanoscale morphology (see Figure S6b, Supporting Information). Given the overall PDPP3T:PCBM volume fractions, this indicates that two coherent polymer lamellae stacks within a polymer-rich mesodomain determine roughly the interface to interface distance to the larger PCBM-rich aggregate phase. Specifically, the size of PCBM-rich and polymer-rich domains has to be similar on account of the similar volume fraction of each component. When polymer crystals are located in-between PCBM domains with face-on orientation as revealed by WAXS with respect to the electrode interface (shown in Figure 3a) the meso-length-scale spacing ξ_2 is about 4 times the nanoscale spacing ξ_3. This novel finding indicates that the mesoscale and nanoscale length scales are determined by the polymer crystallization.

The effect of the morphology manipulated via solvent combinations on device performance is significant for J_{sc} and FF. In contrast, V_{oc} is controlled by the HOMO–LUMO level and does not show a strong morphology dependence. The evolution of J_{sc} and FF as a function of solvents can be explained only to some degree within the classical two phases morphology paradigm. **Figure 4**a shows the correlation of mesoscale ξ_2 with J_{sc}. In general, smaller domains induce higher J_{sc} and larger

Adv. Mater. 2014,
DOI: 10.1002/adma.201400216

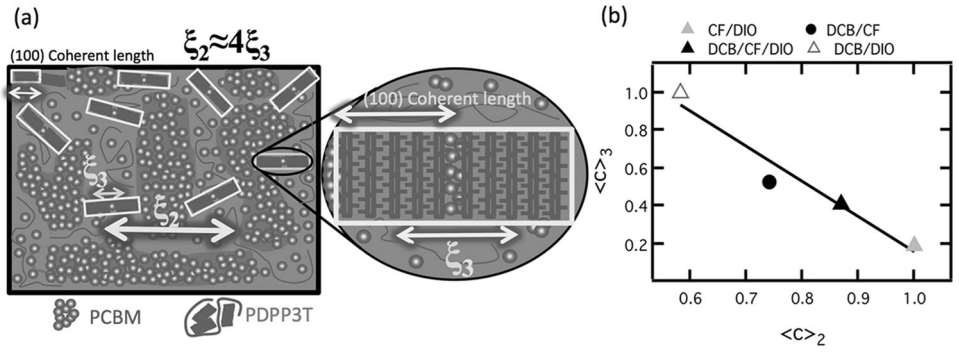

Figure 3. a) Scheme of morphological picture revealed in this work for PDPP3T:$PC_{71}BM$ blend. b) The anti-correlation between relative $<\Delta c>_2$ and relative $<\Delta c>_3$ at different length scales.

domains lead to worse J_{sc}. We note though that the blend films processed with DCB, DCB/CF and DCB/CF/DIO show very similar ξ_2, but J_{sc} is different. This indicates that ξ_2 is not the only factor to control J_{sc}. Given the morphological complexity at hand, two length scales and two composition variations, as well as polymer ordering as inferred from GIWAXS, all parameters must be considered when analyzing the dependence of J_{sc} and FF on the morphology. We will discuss this below when considering separately the photocurrent generated from the PCBM and the polymer, considering yet more variables and complexities that have not been investigated much.

The photo currents $J_{sc:polymer}$ and $J_{sc:PCBM}$ show strong solvent dependency (see Figure 1d). When CF is used, the polymer-generated photocurrent contributes more than $PC_{71}BM$, but when CF is absent, the contributions are reversed. When DIO is used, the quantum yield over the entire spectrum is improved relative to the respective devices w/o DIO. This demonstrates that CF and DIO show different impact on quantum efficiency of polymer and PCBM. CF and CF/DIO exhibit largest and smallest mesoscale ξ_2, and consequently low and high $J_{sc:polymer}$ and $J_{sc:PCBM}$ are obtained. The correlation between $J_{sc:PCBM}$ and the internal characteristic length scale ξ_3 in the polymer-rich nanophase is plotted in Figure 4b. For DCB-based solvents, $J_{sc:PCBM}$ increases as a function of ξ_3. This indicates that a larger phase separation is favorable for exciton dissociation efficiency if the size scale is similar to the exciton diffusion length. This

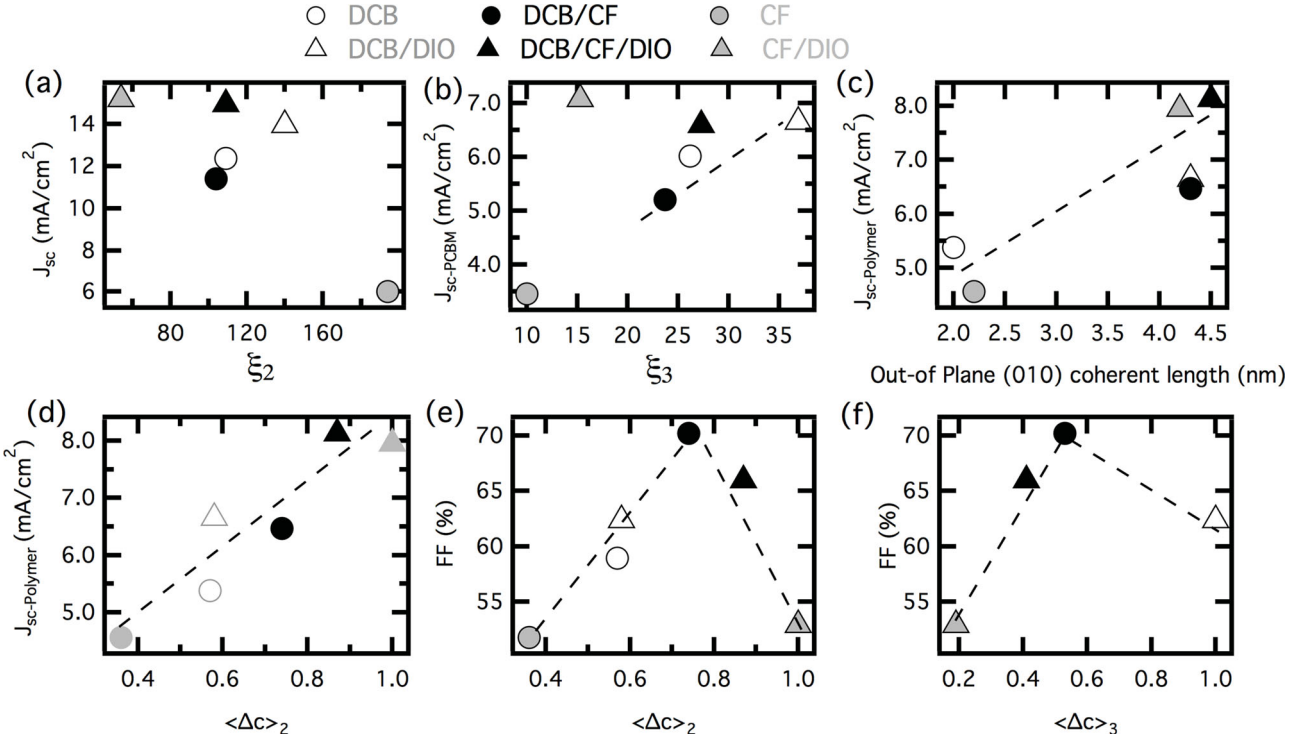

Figure 4. Performance parameters J_{sc} and FF plotted against the characteristic median length scale ξ and the average composition variations $<\Delta c>$ for solvents as indicated. a) J_{sc} as a function of ξ_2, b) $J_{sc-PCBM}$ as a function of ξ_3, c) $J_{sc-Polymer}$ as a function of the out-of plane (010) coherent length for blends processed with different solvents, d) $J_{sc-Polymer}$ as a function of the relative $<\Delta c>_2$, e) FF as a function of the relative $<\Delta c>_2$, f) FF as a function of the relative $<\Delta c>_3$.

DOI: 10.1002/adma.201400216

is consistent with Monte-Carlo simulations, which demonstrates that domains too small induce higher recombination.[44] For $J_{sc:polymer}$, the ranking is DCB < DCB/CF <DCB/CF/DIO, which is consistent with the ranking of the (010) coherence length in the out-of plane direction (the charge transport direction in the device) as revealed by GIWAXS (010) peak (see Figure 4c). This ranking is also consistent with the hole mobility of these three blends.[25] Furthermore, Figure 4d shows the correlation between $<\Delta c>_2$ and $J_{sc:polymer.}$, where $J_{sc:polymer}$ almost linearly increases on average with $<\Delta c>_2$. This indicates that charge transport efficiency is enhanced when fullerene and polymer-rich phase become purer and once the carriers have escaped the recombination in the mixed phase. Most interestingly, the three DCB-based blends that have almost identical ξ_2, are now nicely differentiated by considering the composition variations. We also note that the (010) coherence length is loosely correlated to $<\Delta c>_2$ as purer domains can lead more readily to longer-range order.

The relation of FF with the various device and morphology parameters is complex, as both field-dependent geminate recombination and bimolecular recombination can impact the FF.[60] Our discussion will assume that the field dependent geminate recombination is similar for all devices, and that bimolecular recombination is governed by how fast the charges travel to reach the electrodes (i.e., mobility) and how many recombination sites (impurities/composition variations) they encounter during this time. The relation of FF with $<\Delta c>_2$ is plotted in Figure 4e. A continuous, but non-monotonic evolution is found.[32,46] When mixed domains dominate the devices (films processed with CF), i.e. FF is low as holes and electrons readily recombine in the mixed domains via bimolecular recombination. This is consistent with previously reported work.[23,49] However, the FF initially improves and then drops when the $<\Delta c>_2$ is higher than 0.74 (i.e., blend films processed with CF/DIO showing the second lowest FF and also the highest relative composition variations). The situation is similar when the relation of the compositional variation of the nanophase $<\Delta c>_3$ and FF are considered (Figure 4f, DCB is an exception as mentioned above), the best FF is observed again for intermediate $<\Delta c>_3$. Given that higher $<\Delta c>_2$ corresponds to a lower $<\Delta c>_3$ the observed reverse ordering with respect to the solvent is not surprising.

The hierarchical morphology observed reveals thus a complex impact on device performance. What the ideal a priori composition variations are in a hierarchical system is unclear. Here, the anti-correlation of the mesoscale $<\Delta c>_2$ and nanoscale $<\Delta c>_3$ reveal that FF can be reduced when the compositional variations of either the mesoscale or the nanoscale are too small. Hierarchical structures are thus not intrinsically superior to a monomodal morphology. While hierarchical structures are thought to improve charge separation and transport, our results indicate that additional conditions on purity and transport pathways have to be met for optimal performance. It is unclear what the ideal hierarchical morphology would be, and its delineation might be an interesting subject of advanced modeling to evaluate the impact of ξ_2, ξ_3, $<\Delta c>_2$, and $<\Delta c>_3$ on charge transport and bimolecular recombination.

Regarding the dependence of the morphology on solvent parameters, it is interesting to note that in the host solvent DCB, $<\Delta c>_2$ increases when either CF or DIO is employed, and further increases if both CF and DIO are added. This can be rationalized by the solubility of the materials in the solvents. We measured the solubility of PDPP3T in DCB, CF and DIO and find both CF and DIO are better solvents for PCBM than for PDPP3T (see Figure S7, Supporting Information). However, the strength of the relative solubility limits (as judged by considering ratios) indicates that, compared to DCB, CF is a comparatively poor solvent for PCBM and DIO is a poor solvent for the polymer. Hence, when added to DCB, 20% CF strongly purifies the polymer phase and 5% DIO purifies both the polymer domains and the PCBM aggregates.

In summary, we have quantified for the first time the composition variations in a complex three-phase, hierarchical morphology using PDPP3T:$PC_{71}BM$ devices and established novel structure–function relations that include separate consideration of the EQE of the polymer and fullerene components. We have revealed a structural relation between inter-polymer molecular ordering and composition variations with a novel R-SoXS analysis method. Furthermore, anti-correlated composition variations are found between mesoscale and nanoscale structures that determine the FF. High composition variations cannot be achieved simultaneously at the two different length scales and consequently the highest FF is obtained for a morphology that is a compromise between the competition of the different length scales. Similarly, the photocurrent generated from fullerene or polymer is intimately linked to the complex morphology, but neither of the two currents is optimized by the same morphology, nor for the morphology that gives the highest FF. Thus, although PDPP3T:$PC_{71}BM$ devices reached a PCE of 6.7% by processing the blends with DCB/CF/DIO ternary solvent,[25] and this PCE is one of the highest reported for DPP based blends;[61] the three-phase morphology revealed here is not ideal yet. None of the solvent mixtures simultaneously optimize FF, J_{sc} and V_{oc} and overall, the IQE, particularly of the polymer, is poor. Further improvements of this material system should be possible. The results suggest that the strong aggregation of high molecular weight PDPP3T and low fullerene miscibility might be detrimental and needs to be controlled and moderated through improved fabrication methods, and/or reduced molecular weight or side-chain modifications of the polymer. Importantly, our results point out that hierarchical structures are very complex and delineation of an ideal hierarchical morphology requires significant additional research.

Experimental Section

Materials: PDPP3T (M_n = 780 kg/mol, PDI = 3.25) was purchased from Solarmer Material Inc. and $PC_{71}BM$ was purchased from Nano-C. The ultra dry solvents used in device fabrication process were purchased from Alfa Aesar. The solvents used are CF, DCB, DCB/CF (4:1), CF/DIO (DIO 5% v), DCB/DIO (DIO 5% v) and DCB/CF/DIO (4:1, DIO 5% v). The other chemicals are commercial available products and used without any further purification.

Measurements: The thickness of the active layer was controlled by changing the spin speed during the spin-coating process and measured on profilometer (Ambios Tech. XP-2). GIWAXS,R-SoXS,and reference spectroscopy/miscibility measurements were performed at beamline 7.3.3,[62] beamline 11.0.1.2,[63] and beamline 5.3.2.2,[57] respectively, at the Advanced Light Source, Lawrence Berkeley National Laboratory, Berkeley, CA. EQE measurements were performed at Solar Cell Spectral Response Measurement System QE-R3011 (Enli Technoloy Co. Ltd).

Adv. Mater. 2014,
DOI: 10.1002/adma.201400216

The *J–V* curves were measured under the illumination of 100 mW/cm^2 AM 1.5G using a XES-70S1 (SAN-EI Electric Co., Ltd.) solar simulator (AAA grade, 70 mm × 70 mm photo-beam size). The 2 cm × 2 cm monocrystalline silicon reference cell (SRC-1000-TC-QZ) was purchased from VLSI Standards Inc.

Supporting Information

Supporting Information is available from the Wiley Online Library or from the author.

Acknowledgements

X-ray characterization, device fabrication, and device measurements by NCSU were supported by the U.S. Department of Energy, Office of Science, Basic Energy Science, Division of Materials Science and Engineering under Contract DE-FG02–98ER45737. X-ray data was acquired at beamlines 11.0.1.2, 7.3.3 and 5.3.2.2 at the Advanced Light Source, which is supported by the Director, Office of Science, Office of Basic Energy Sciences, of the U.S. Department of Energy under Contract No. DE-AC02–05CH11231. The authors would like to acknowledge financial support from the National High Technology Research and Development Program 863 (2011AA050523), the Chinese Academy of Sciences, the Ministry of Science and Technology of China, and the NSFC (Nos. S2012GR0224, 51173189).

Received: January 14, 2014
Revised: February 9, 2014
Published online:

[1] T. Agostinelli, S. Lilliu, J. G. Labram, M. Campoy-Quiles, M. Hampton, E. Pires, J. Rawle, O. Bikondoa, D. D. C. Bradley, T. D. Anthopoulos, J. Nelson, J. E. Macdonald, *Adv. Funct. Mater.* **2011**, *21*, 1701–1708.
[2] T. L. Benanti, D. Venkataraman, *Photosynth. Res.* **2006**, *87*, 73–81.
[3] C.-Y. Chang, Y.-J. Cheng, S.-H. Hung, J.-S. Wu, W.-S. Kao, C.-H. Lee, C.-S. Hsu, *Adv. Mater.* **2012**, *24*, 549–553.
[4] D. Chen, A. Nakahara, D. Wei, D. Nordlund, T. P. Russell, *Nano Lett.* **2011**, *11*, 561–567.
[5] W. Chen, T. Xu, F. He, W. Wang, C. Wang, J. Strzalka, Y. Liu, J. Wen, D. J. Miller, J. Chen, K. Hong, L. Yu, S. B. Darling, *Nano Lett.* **2011**, *11*, 3707–3713.
[6] B. A. Collins, J. E. Cochran, H. Yan, E. Gann, C. Hub, R. Fink, C. Wang, T. Schuettfort, C. R. McNeill, M. L. Chabinyc, H. Ade, *Nat. Mater.* **2012**, *11*, 536–543.
[7] B. A. Collins, H. Ade, *J. Electron Spectrosc. Relat. Phenom.* **2012**, *185*, 119–128.
[8] B. A. Collins, J. R. Tumbleston, H. Ade, *J. Phys. Chem. Lett.* **2011**, *2*, 3135–3145.
[9] X. He, B. A. Collins, B. Watts, H. Ade, C. R. McNeill, *Small* **2012**, *8*, 1920–1927.
[10] A. Herzing, L. J. Richter, I. M. Anderson, *J. Phys. Chem. C* **2010**, *114*, 17501–17508.
[11] C. R. McNeill, H. Ade, *J. Mater. Chem. C* **2013**, *1*, 187–201.
[12] B. P. Rand, D. Cheyns, K. Vasseur, N. C. Giebink, S. Mothy, Y. Yi, V. Coropceanu, D. Beljonne, J. Cornil, J.-L. Brédas, J. Genoe, *Adv. Funct. Mater.* **2012**, *22*, 2987–2995.
[13] B. A. Collins, Z. Li, J. R. Tumbleston, E. Gann, C. R. McNeill, H. Ade, *Adv. Energy Mater.* **2013**, *3*, 65–74.
[14] L. Dou, J. You, J. Yang, C.-C. Chen, Y. He, S. Murase, T. Moriarty, K. Emery, G. Li, Y. Yang, *Nat. Photonics* **2012**, *6*, 180–185.
[15] Z. He, C. Zhong, S. Su, M. Xu, H. Wu, Y. Cao, *Nat. Photonics* **2012**, *6*, 591–595.
[16] H.-Y. Chen, J. Hou, S. Zhang, Y. Liang, G. Yang, Y. Yang, L. Yu, Y. Wu, G. Li, *Nat. Photonics* **2009**, *3*, 649–653.
[17] G. Li, R. Zhu, Y. Yang, *Nat. Photonics* **2012**, *6*, 153–161.
[18] G. Li, V. Shrotriya, J. Huang, Y. Yao, T. Moriarty, K. Emery, Y. Yang, *Nat. Mater.* **2005**, *4*, 864–868.
[19] J. Chen, Y. Cao, *Acc. Chem. Res.* **2009**, *42*, 1709–1718.
[20] D. Qian, W. Ma, Z. Li, X. Guo, S. Zhang, L. Ye, H. Ade, Z. Tan, J. Hou, *J. Am. Chem. Soc.* **2013**, *135*, 8464–8467.
[21] X. Guo, M. Zhang, J. Tan, S. Zhang, L. Huo, W. Hu, Y. Li, J. Hou, *Adv. Mater.* **2012**, *24*, 6536–6541.
[22] W. Ma, J. Y. Kim, K. Lee, A. J. Heeger, *Macromol. Rapid Commun.* **2007**, *28*, 1776–1780.
[23] W. Ma, J. Tumbleston, M. Wang, E. Gann, F. Huang, H. Ade, *Adv. Energy Mater.* **2013**, *3*, 864–872.
[24] G. Li, Y. Yao, H. Yang, V. Shrotriya, G. Yang, Y. Yang, *Adv. Funct. Mater.* **2007**, *17*, 1636–1644.
[25] L. Ye, S. Zhang, W. Ma, B. Fan, X. Guo, Y. Huang, H. Ade, J. Hou, *Adv. Mater.* **2012**, *24*, 6335–6341.
[26] J. Peet, J. Y. Kim, N. E. Coates, W. L. Ma, D. Moses, a. J. Heeger, G. C. Bazan, *Nat. Mater.* **2007**, *6*, 497–500.
[27] V. D. Mihailetchi, H. X. Xie, B. de Boer, L. J. A. Koster, P. W. M. Blom, *Adv. Funct. Mater.* **2006**, *16*, 699–708.
[28] P. E. Shaw, A. Ruseckas, I. D. W. Samuel, *Adv. Mater.* **2008**, *20*, 3516–3520.
[29] L.-J. Zuo, X.-L. Hu, T. Ye, T. R. Andersen, H.-Y. Li, M.-M. Shi, M. Xu, J. Ling, Q. Zheng, J.-T. Xu, E. Bundgaard, F. C. Krebs, H.-Z. Chen, *J. Phys. Chem. C* **2012**, *116*, 16893–16900.
[30] B. Walker, A. Tamayo, D. T. Duong, X.-D. Dang, C. Kim, J. Granstrom, T.-Q. Nguyen, *Adv. Energy Mater.* **2011**, *1*, 221–229.
[31] J. T. Rogers, K. Schmidt, M. F. Toney, E. J. Kramer, G. C. Bazan, *Adv. Mater.* **2011**, *23*, 2284–2288.
[32] W. Yin, M. Dadmun, *ACS Nano* **2011**, *5*, 4756–4768.
[33] F. C. Jamieson, E. B. Domingo, T. McCarthy-Ward, M. Heeney, N. Stingelin, J. R. Durrant, *Chem. Sci.* **2012**, *3*, 485–492.
[34] J. A. Bartelt, Z. M. Beiley, E. T. Hoke, W. R. Mateker, J. D. Douglas, B. A. Collins, J. R. Tumbleston, K. R. Graham, A. Amassian, H. Ade, J. M. J. Frechet, M. F. Toney, M. D. McGehee, *Adv. Energy Mater.* **2013**, *3*, 364–374.
[35] M. Pfannmöller, H. Flügge, G. Benner, I. Wacker, C. Sommer, M. Hanselmann, S. Schmale, H. Schmidt, F. Hamprecht, T. Rabe, W. Kowalsky, R. R. Schröder, *Nano Lett.* **2011**, *11*, 3099–3107.
[36] N. D. Treat, M. Brady, G. Smith, M. F. Toney, E. J. Kramer, C. J. Hawker, M. L. Chabinyc, *Adv. Energy Mater.* **2011**, *1*, 82–89.
[37] B. A. Collins, E. Gann, L. Guignard, X. He, C. R. McNeill, H. Ade, *J. Phys. Chem. Lett.* **2010**, *1*, 3160–3166.
[38] N. D. Treat, A. Varotto, C. J. Takacs, N. Batara, M. Al-hashimi, M. J. Heeney, A. J. Heeger, F. Wudl, C. J. Hawker, M. L. Chabinyc, *J. Am. Chem. Soc.* **2012**, *134*, 15869–15879.
[39] B. W. Boudouris, V. Ho, L. H. Jimison, M. F. Toney, A. Salleo, R. A. Segalman, *Macromolecules* **2011**, *44*, 6653–6658.
[40] A. C. Mayer, M. F. Toney, S. R. Scully, J. Rivnay, C. J. Brabec, M. Scharber, M. Koppe, M. Heeney, I. McCulloch, M. D. McGehee, *Adv. Funct. Mater.* **2009**, *19*, 1173–1179.
[41] J. L. Bredas, R. Silbey, D. S. Boudreaux, R. R. Chance, *J. Am. Chem. Soc.* **1983**, *371*, 6555–6559.
[42] O. G. Reid, J. a. N. Malik, G. Latini, S. Dayal, N. Kopidakis, C. Silva, N. Stingelin, G. Rumbles, *J. Polym. Sci., Part B: Polym. Phys.* **2012**, *50*, 27–37.
[43] R. R. Lunt, N. C. Giebink, A. A. Belak, J. B. Benziger, S. R. Forrest, *J. Appl. Phys.* **2009**, *105*, 053711.

[44] B. P. Lyons, N. Clarke, C. Groves, *Energy Environ. Sci.* **2012**, *5*, 7657–7663.
[45] F. Reisdorffer, O. Haas, P. Le Rendu, T. P. Nguyen, *Synth. Met.* **2012**, *161*, 2544–2548.
[46] S. Albrecht, S. Janietz, W. Schindler, J. Frisch, J. Kurpiers, J. Kniepert, S. Inal, P. Pingel, K. Fostiropoulos, N. Koch, D. Neher, *J. Am. Chem. Soc.* **2012**, *134*, 14932–14944.
[47] S. Bertho, W. D. Oosterbaan, V. Vrindts, J. D'Haen, T. J. Cleij, L. Lutsen, J. Manca, D. Vanderzande, *Org. Electron.* **2009**, *10*, 1248–1251.
[48] F. Liu, Y. Gu, C. Wang, W. Zhao, D. Chen, A. L. Briseno, T. P. Russell, *Adv. Mater.* **2012**, *24*, 3947–3951.
[49] A. Stuart, J. R. Tumbleston, H. Zhou, H. Ade, W. Li, W. You, *J. Am. Chem. Soc.* **2013**, *135*, 1806–1815.
[50] H. Yan, S. Swaraj, C. Wang, I. Hwang, N. C. Greenham, C. Groves, H. Ade, C. R. McNeill, *Adv. Funct. Mater.* **2010**, *20*, 4329–4337.
[51] W. Ma, L. Ye, S. Zhang, J. Hou, H. Ade, *J. Mater. Chem. C* **2013**, *1*, 5023–5030.
[52] S. Swaraj, C. Wang, H. Yan, B. Watts, J. Lüning, C. R. McNeill, H. Ade, *Nano Lett.* **2010**, *10*, 2863–2869.
[53] H. Yan, B. A. Collins, E. Gann, C. Wang, H. Ade, *ACS Nano* **2012**, *6*, 677–688.
[54] M. Turbiez, D. M. De Leeuw, A. J. Janssen, *J. Am. Chem. Soc.* **2009**, *131*, 16616–16617.
[55] C. Guo, Y. Lin, M. D. Witman, K. A. Smith, C. Wang, A. Hexemer, J. Strzalka, E. D. Gomez, R. Verduzco, *Nano Lett.* **2013**, *13*, 2957–2963.
[56] T. Coffey, S. Urquhart, H. Ade, *J. Electron Spectrosc. Relat. Phenom.* **2002**, *122*, 65–78.
[57] A. L. D. Kilcoyne, T. Tyliszczak, W. F. Steele, S. Fakra, P. Hitchcock, K. Franck, E. Anderson, B. Harteneck, E. G. Rightor, G. E. Mitchell, A. P. Hitchcock, L. Yang, T. Warwick, H. Ade, *J. Synchrotron Radiat.* **2003**, *10*, 125–136.
[58] B. A. Collins, Z. Li, C. R. McNeill, H. Ade, *Macromolecules* **2011**, *44*, 9747–9751.
[59] N. Stribeck, *X-Ray Scattering of Soft Matter*, Springer, Heidelberg, Germany **2007**.
[60] S. Albrecht, W. Schindler, J. Kurpiers, J. Kniepert, J. C. Blakesley, I. Dumsch, S. Allard, K. Fostiropoulos, U. Scherf, D. Neher, *J. Phys. Chem. Lett.* **2012**, *3*, 640–645.
[61] W. Li, A. Furlan, K. H. Hendriks, M. M. Wienk, R. A. J. Janssen, *J. Am. Chem. Soc.* **2013**, *135*, 5529–5532.
[62] A. Hexemer, W. Bras, J. Glossinger, E. Schaible, E. Gann, R. Kirian, A. MacDowell, M. Church, B. Rude, H. Padmore, *J. Phys. Conf. Ser.* **2010**, *247*, 012007.
[63] E. Gann, A. T. Young, B. A. Collins, H. Yan, J. Nasiatka, H. A. Padmore, H. Ade, A. Hexemer, C. Wang, *Rev. Sci. Instrum.* **2012**, *83*, 045110.

Adv. Mater. **2014**,
DOI: 10.1002/adma.201400216